Journal of Applied Fluid Mechanics, Vol. 16, No. 8, pp. 1615-1626, 2023.
Available online at www.jafmonline.net, ISSN 1735-3572, EISSN 1735-3645.
https://doi.org/10.47176/jafm.16.08.1741

Effects of Volute Structure on Energy Performance and Rotor Operational Stability of Molten Salt Pumps

Q. Li[1], R. Zhang[2†] and H. Xu[2]

[1] *College of Water Conservancy and Hydropower Engineering, Hohai University, Nanjing 210098, China*
[2] *College of Agricultural Science and Engineering, Hohai University, Nanjing 211100, China*

†*Corresponding Author Email: gulie1984@163.com*

ABSTRACT

A double-volute molten salt pump with two outlet pipes is proposed based on the original pump model. A numerical approach coupling finite element analysis and computational fluid dynamics (CFD) is implemented to investigate the operational stability and energy performance of two molten salt centrifugal pumps for high-temperature molten salt. The entropy production of the single-volute and double-volute molten salt pumps is investigated. The effects of the volute structures on the mechanical behavior of the impeller and shaft are considered. According to the findings, the local entropy production in the molten salt pump is dominated by the local pulsating entropy production (Spro-T), with the double-volute scheme achieving reduced energy loss. A visualization of the flow field and the local entropy production rate (LEPR) distributions indicate that the LEPR is positively correlated with the complexity of the flow, and higher levels of turbulence intensity lead to greater LEPR. The double-volute scheme enhances the complexity of the flow in the impeller, resulting in an increase in the LEPR compared with the single-volute design. However, the LEPR in the whole double-volute molten salt pump is reduced compared with the single-volute design. It is discovered that the double-volute molten salt pump experiences a less radial hydraulic force. Although the double-volute design has a slightly higher maximum equivalent stress on the impeller than the single-volute scheme, the rotor deformation is significantly less. In general, the double-volute scheme reduces energy loss and ensures better structural stability.

Article History
Received January 4, 2023
Revised March 13, 2023
Accepted April 3, 2023
Available online May 31, 2023

Keywords:
Molten salt pump
Entropy production theory
Multi-field coupling
Double volute
Rotor

1. INTRODUCTION

High-temperature centrifugal molten salt pumps are commonly used in solar thermal storage power plant systems to transport molten salt at temperatures above 700 K. It is generally that the pumps are submerged in the high-temperature molten salt and installed vertically in a tank. This working environment is relatively harsh (Barth et al., 2002). Furthermore, the pump rotor components are affected by the flow field and are prone to structural deformation and vibration (Egusquiza et al., 2012; Zhang et al., 2020). Once the molten salt pump can no longer operate continuously, the molten salt will rapidly solidify, potentially clogging the pipework of the system (Zhou et al., 2020). Thus, ensuring the continuous and stable operation of molten salt pumps is as important as maintaining good performance. Currently, the study of high-temperature pumps concentrates on two aspects: analyzing the flow field inside of a pump while transporting high-temperature molten salt (Cheng et al., 2017a) and analyzing the fluid–thermal–structure coupling of a pump to explore the deformation and equivalent stress of the rotor caused by the high-temperature flow field (Kang et al., 2020).

The physical properties of molten salts, such as their viscosity and density, differ at different temperatures. It is challenging to identify the flow field of molten salt pumps in laboratories using optical flow measurement technology because of the high temperature of the medium. It is feasible to see the flow in a pump while it is transporting a high-temperature medium by numerical simulation. Cheng et al. (2019) explored the unsteady features of the flow field of molten salt pumps at various viscosities. They identified the mechanism of flow loss in relation to viscosity using CFD. Gu et al. (2022) studied the vortical flow and transient pressure pulsations in a molten salt pump, enabling better design and safer operation of the pump. Shao and Zhao (2017) suggested a method for conducting molten salt pump experiments with water rather than molten salt through dimensionless numerical analysis.

Unlike ordinary centrifugal pumps, it is not only the

Nomenclature

b_2	impeller outlet width	D_{dd}	double-volute pump outlet diameter
b_z	volute inlet width	D_{ds}	single-volute pump outlet diameter
D_1	impeller inlet diameter	H	pump head
D_2	impeller outlet diameter	n	rotation speed
D_3	volute base circle diameter	q_v	flow rate

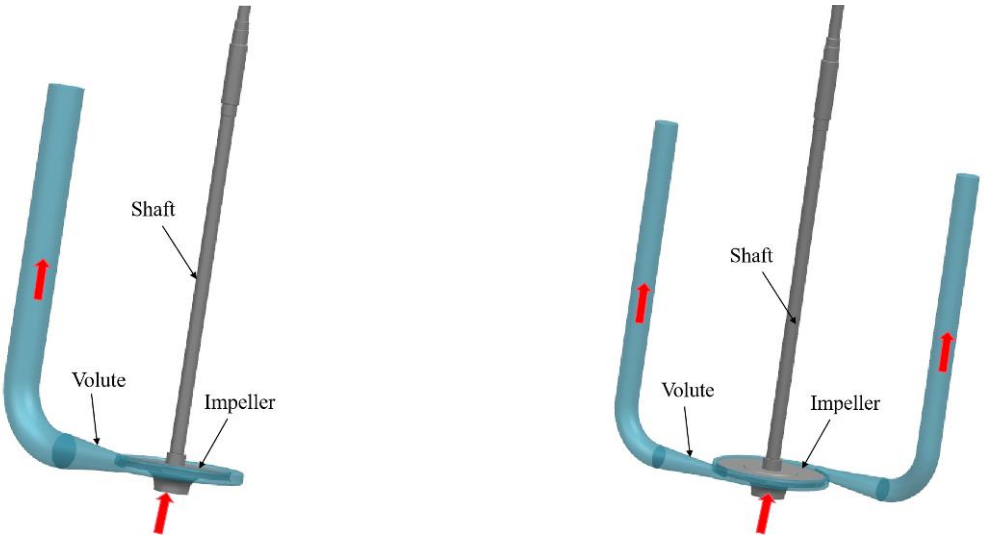

(a) Single volute (b) Double volute

Fig. 1. Centrifugal molten salt pump schemes

flow characteristics of molten salt pumps that must be considered under high-temperature conditions (Cheng et al., 2017b). Additionally, it is essential to analyze the deformation and stress experienced by the impeller and shaft when the pump operates in high-temperature conditions. For this, fluid–thermal–structure coupling is required (Pei et al., 2014). Kang et al. (2020) and Teng et al. (2020) adopted a fluid–thermal-structure coupling strategy to load the CFD and thermal analysis results onto the pump rotor for finite element analysis to investigate the stress and deformation of the rotor. Because of this, it was possible to describe the factors that influence the operational reliability of the rotor.

Research on energy loss in fluid machinery has been conducted based on energy conversion theory in recent years. The flow characteristics and energy performance of a pump under cavitation conditions were revealed by applying the entropy production theory (Fei et al., 2022). Gu et al. (2019) studied the flow loss of the high-power pump by numerical visualization method to improve the pump's hydraulic performance. Moreover, the energy conversion theory is frequently utilized in the study of hydraulic turbines, which may be used as a reference.

Although the flow field and structural stability of molten salt pumps have been extensively examined, the structural parameters of molten salt pumps have rarely been optimized. Furthermore, the flow field distribution in molten salt pumps is the primary means of energy loss, but there have been few visual investigations of this phenomenon. The successful application of entropy production theory provides a new approach to studying the energy characteristics of molten salt pumps.

In this study, two molten salt pumps are designed, namely single-volute and double-volute structures. The objectives of this study are to explore the operational stability and energy performance of these two centrifugal pump schemes for transporting high-temperature molten salt. The flow characteristic and energy performance are investigated using the entropy production theory and CFD method. We can explain the correlation between the flow field distribution and energy loss and identify the optimal volute structure for better energy performance of the pump. Furthermore, a coupling strategy is designed, and the load on the rotor for the finite element analysis is the pressure distribution derived from the results of CFD. The structural characteristics of the shaft and impeller under the two schemes are analyzed to clarify the deformation and stress on the rotor. The results presented herein are expected to be a reference for the most efficient design of a molten salt pump and its consistent functioning.

2. NUMERICAL MODELS AND METHOD

2.1 Numerical Models

The fluid domain of the molten salt pump established for numerical calculations is displayed in Fig. 1. Figure 1 (a) shows the fluid calculation domain of a single-volute pump, including the volute, impeller, and outlet pipe. The double volute structure is a new design paired with two outlet pipes and is a circumferential symmetrical structure with two tongues, as shown in Fig. 1(b). It is

Table 1 Structural parameters of impeller and volute.

Parameter	Value
Impeller	
inlet diameter, D_1/mm	140
outlet diameter, D_2/mm	464
outlet width, b_2/mm	16
blades, Z	6
Single volute	
base circle diameter, D_3/mm	480
inlet width, b_z/mm	40
outlet diameter, D_{ds}/mm	150
Double volute	
base circle diameter, D_3/mm	480
inlet width, b_z/mm	40
outlet diameter, D_{dd}/mm	100

anticipated that the double-volute design would mitigate the resultant radial hydraulic loaded on the pump. The two molten salt pumps share an impeller and shaft. The structural parameters are listed in Table 1. The molten salt pumps of both schemes operate at the nominal flow rate of q_v=200 m^3/h, with a rotation speed of n=1450 RPM and a pump head of H=65 m under the design conditions.

2.2 Medium properties

The binary molten nitrate (60% by weight $NaNO_3$ and 40% by weight KNO_3) commonly used in photothermal power generation is selected as the fluid medium (Smith et al., 1994; Peiró et al., 2017). Numerical simulations were performed with the two molten salt pump schemes using water, 573 K molten salt, 723 K molten salt, and 838 K molten salt. The density and viscosity of molten salt at different temperatures are presented in Table 2.

2.3 Numerical Method

(1) Turbulence Model and Boundary Conditions

The flow in the molten salt pump adheres to the physical conservation law and is assumed incompressible according to the properties listed in Table 2 (Huan et al., 2021; Li et al., 2019). The SST $k-\omega$ turbulence model is selected for the closure of the flow governing equation based on the Reynolds-average Navier–Stokes (RANS) (Moshfeghi et al., 2012; Shao et al., 2015, 2019; Kang et al., 2020; Kumar et al,. 2022). This model allows the RANS equations to be solved for the flow and is suitable for the rotating fluid machinery (Kang et al., 2017; Lin et al., 2021). The flow field in the pump is resolved using the commercial software ANSYS CFX 18.0 (Kang et al., 2022).

Table 2 Physical properties of the molten salt

Physical properties	573 K molten	723 K molten	838 K molten salt	water
Density /kg/m^3	1899	1 804	1 730	997
Viscosity /Pa·s	0.00 326	0.00 147	0.00 114	0.00 089

The velocity inlet boundary condition is imposed at the pump inlet. The boundary condition of the pump outlet is given the outflow. All flow parameters except static pressure are subject to a zero normal gradient. The internal surfaces of the pump wetted by molten salt are given a 0.025 mm surface roughness and no-slip boundary conditions. The standard wall function is used to address areas that are near-wall regions.

(2) Grid Independence Examination

Grid research was carried out at 1.0q_v to lessen the influence of the grid cell count on the numerical calculation. With resolutions for a single-volute pump ranging from 1.26×10^6 to 3.27×10^6 and a double-volute pump from 1.29×10^6 to 3.91×10^6, five grid schemes were created, respectively. The same numerical strategy was applied to all five grid schemes for the single-volute and double-volute molten salt pumps. The head was obtained by taking the pressure at the pump inlet and outlet. Figure 2 displays a plotting of the head of two pumps under five grid schemes respectively. The number of grid cells exceeds 2.24×10^6 for the single-volute pump and 2.62×10^6 for the double-volute pump, the relative deviation in the pump head is slight. The schemes with total grid numbers of 2.24×10^6 (single-volute pump) and 2.62×10^6 (double-volute pump) were selected for subsequent simulations in order to balance accuracy and computing efficiency.

(3) Physical Validity Examination

The molten salt pump with a single volute was investigated by numerical simulation at three typical water flow rates of 0.8q_v, 1.0q_v, and 1.2q_v. The head and

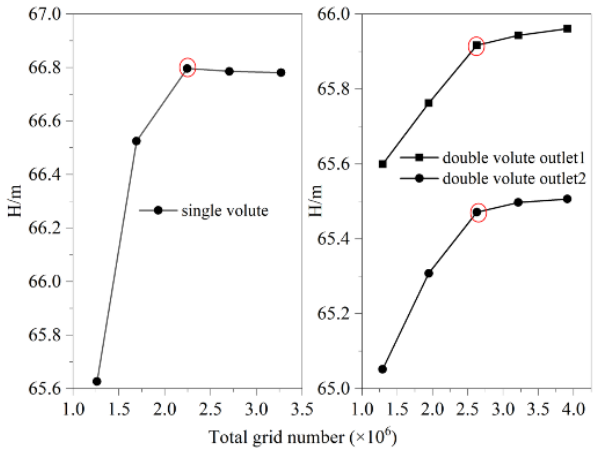

Fig. 2. Grid independence study of the two pumps.

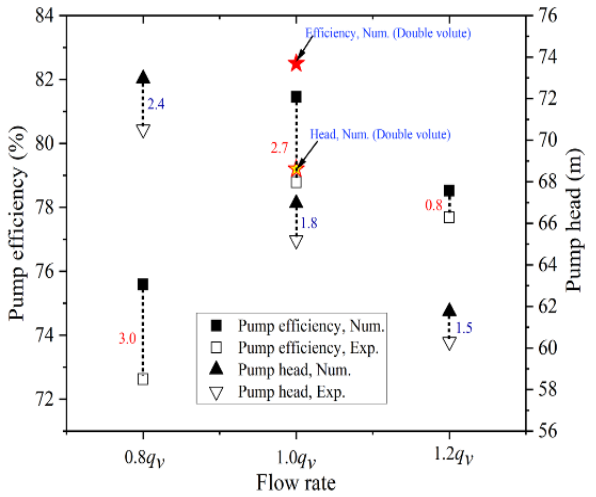

Fig. 3. Experimental (Exp.) and numerical (Num.) results for the head and efficiency

efficiency obtained numerically and experimentally are compared in Fig. 3. The numerical simulation results are greater than the experimental results under the three flow rates. The maximum deviations in terms of the efficiency and head of the pump occur at 0.8q_v, which is 4.1% and 3.5%, respectively. This deviation occurs because the boundary conditions in the numerical simulations are slightly inconsistent with the test conditions; however, the deviation is within a reasonable range. These results demonstrate the validity of the numerical method. In addition, the head and efficiency of the double-volute scheme are higher than those of the single-volute scheme at the design condition. This proves that the double-volute pump satisfies the design requirements and improves the performance of the pump.

3. ENERGY PERFORMANCE ANSLYSIS

3.1 Entropy Production Analysis Method

Entropy production is essentially a form of energy loss, considered as the irreversible internal energy of mechanical energy conversion in fluid machinery, which is then dissipated. There are many reasons for energy loss within fluid machinery, such as vortices, turbulence, etc. The local entropy production rate (LEPR) includes the local pulsating entropy production rate (LEPR-T) of the pulsating velocity and the local direct entropy production rate (LEPR-D) of the time-averaged velocity. According to the viscosity dissipation function, the LEPR equation of turbulent flow is as follows (Duan et al., 2015; Yu et al., 2022):

$$S_D = S_{\bar{D}} + S_{D'} = \frac{\Phi}{T} \tag{1}$$

$$\Phi = \mu\left\{\begin{array}{l}\left(\frac{\partial u_2}{\partial x_1}+\frac{\partial u_1}{\partial x_2}\right)^2+\left(\frac{\partial u_3}{\partial x_1}+\frac{\partial u_1}{\partial x_3}\right)^2+\left(\frac{\partial u_2}{\partial x_3}+\frac{\partial u_3}{\partial x_2}\right)^2 \\ -\frac{2}{3}\left(\frac{\partial u_1}{\partial x_1}+\frac{\partial u_2}{\partial x_2}+\frac{\partial u_3}{\partial x_3}\right)^2+2\left[\left(\frac{\partial u_1}{\partial x_1}\right)^2+\left(\frac{\partial u_2}{\partial x_2}\right)^2+\left(\frac{\partial u_3}{\partial x_3}\right)^2\right]\end{array}\right\} \tag{2}$$

where Φ is the viscosity dissipation function; T is the temperature; u is the velocity; and μ is the viscosity coefficient.

The LEPR-D equation for an incompressible fluid can be written as (Kock & Herwig, 2004)

$$\frac{\partial u_1}{\partial x_1}+\frac{\partial u_2}{\partial x_2}+\frac{\partial u_3}{\partial x_3}=0 \tag{3}$$

$$S_{\bar{D}} = \frac{\mu}{T}\left\{\begin{array}{l}\left(\frac{\partial u_2}{\partial x_1}+\frac{\partial u_1}{\partial x_2}\right)^2+\left(\frac{\partial u_3}{\partial x_1}+\frac{\partial u_1}{\partial x_3}\right)^2+\left(\frac{\partial u_2}{\partial x_3}+\frac{\partial u_3}{\partial x_2}\right)^2 \\ +2\left[\left(\frac{\partial u_1}{\partial x_1}\right)^2+\left(\frac{\partial u_2}{\partial x_2}\right)^2+\left(\frac{\partial u_3}{\partial x_3}\right)^2\right]\end{array}\right\} \tag{4}$$

The LEPR-T equation for an incompressible fluid can be written as (Kock & Herwig, 2005)

$$S_{D'} = \frac{\mu}{T}\left\{\begin{array}{l}\left(\frac{\partial u_2'}{\partial x_1}+\frac{\partial u_1'}{\partial x_2}\right)^2+\left(\frac{\partial u_3'}{\partial x_1}+\frac{\partial u_1'}{\partial x_3}\right)^2+\left(\frac{\partial u_2'}{\partial x_3}+\frac{\partial u_3'}{\partial x_2}\right)^2 \\ +2\left[\left(\frac{\partial u_1'}{\partial x_1}\right)^2+\left(\frac{\partial u_2'}{\partial x_2}\right)^2+\left(\frac{\partial u_3'}{\partial x_3}\right)^2\right]\end{array}\right\} \tag{5}$$

Note that the pulsating velocity cannot be obtained in the RANS model. The approximate calculation equation of LEPR-T can be written as

$$S_{D'} = \beta\frac{\rho\omega k}{T} \tag{6}$$

where ω represents the turbulent eddy frequency; k represents the turbulent kinetic energy; and β=0.09.

The local direct entropy production (Spro-D) and local pulsating entropy production (Spro-T) are obtained by volume integration of LEPR-D and LEPR-T, respectively. Therefore, the local entropy production equation can be written as

$$\begin{aligned} S_{pro} &= S_{pro-T} + S_{pro-D} \\ &= \int_V S_{D'}dV + \int_V S_{\bar{D}}dV \end{aligned} \tag{7}$$

3.2 Entropy Production of Molten Salt Pump

The volume-averaged LEPRs in the impeller and volute for the single- and double-volute schemes are obtained according to Eqs. (4) and (5) with 573 K molten salt, 723 K molten salt, 838 K molten salt, and water based on the numerical simulation results. At a flow rate of 1.0q_v, the volume-averaged LEPRs are compared in Fig. 4. Whether transporting water or different temperature molten salts, the volume-averaged LEPR in the volute of the two pumps is significantly higher than in the impeller. The double-volute design produces a lower volume-averaged LEPR in the volute and a higher volume-averaged LEPR in the impeller than the single-volute scheme. This result may be owing to the modification of the flow structure by the double volute. As shown in Table 2 and Fig. 4, with the increase of molten salt temperature, the viscosity coefficient decreases, and the volume-average LEPR in the volute and impeller of the two pumps decreases. Note that the gap between the volume-averaged LEPR of the different schemes decreases in the impeller and volute as the molten salt temperature increases.

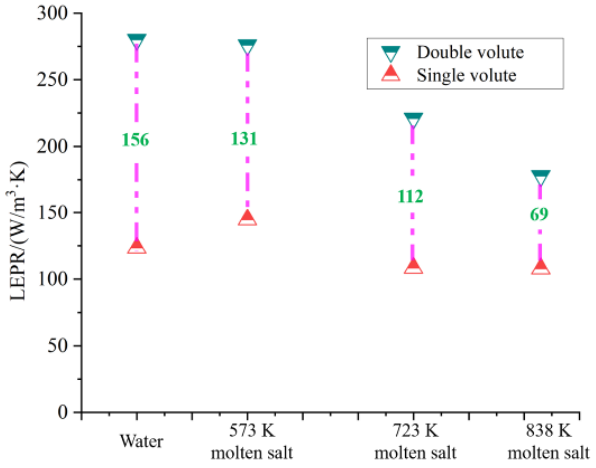

(a) mpeller

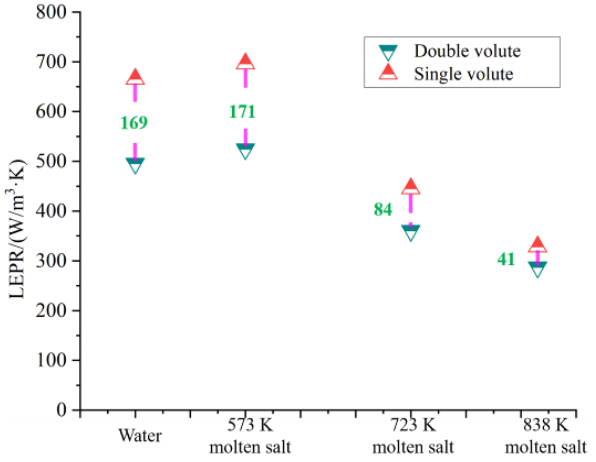

(b) Volute

Fig. 4. Comparison of average LEPR between single- and double-volute schemes

To further illustrate the energy dissipation in molten salt pumps, the LEPR-T and LEPR-D in the volute and impeller were volume-integrated to obtain the entropy production in each component. The results are presented in Table 3. According to Eqs. (4) and (5), the molten salt viscosity coefficient is positively correlated with the LEPR. Therefore, the $S_{pro\text{-}D}$ and $S_{pro\text{-}T}$ decrease with decreasing viscosity. From Table 3, the $S_{pro\text{-}T}$ accounts for a large proportion of the entropy production, and the $S_{pro\text{-}D}$ can be neglected. Therefore, the flow loss is primarily attributed to turbulent dissipation. The entropy production in the volute of the double-volute scheme is lower than that of the single-volute scheme, whereas the entropy production in the impeller exhibits the opposite trend. In general, the total local entropy production of the double-volute molten salt pump is lower than that of the single-volute pump.

4. CHARACTERISTICS OF THE FLOW FIELD

According to the above discussion of energy characteristics, the comparison of the entropy production in the single-volute and double-volute molten salt pumps is consistent under four different mediums. The same conclusion was reached by Jin et al. (2022), i.e., that the properties of the molten salt have an insignificant effect on the energy loss distribution. Therefore, only one molten salt medium (723 K molten salt) is selected for comparative analysis of the flow field and energy performance of the two pumps.

Table 3 Local direct entropy production (Spro-D) and local pulsating entropy production (Spro-T) in impeller and volute (W/K)

(a) Double volute

	$S_{pro\text{-}D}$		$S_{pro\text{-}T}$	
	impeller	volute	impeller	volute
water	0.003	0.003	1.286	2.475
573 K molten salt	0.005	0.005	1.265	2.618
723 K molten salt	0.002	0.002	1.015	1.800
838 K molten salt	0.001	0.001	0.817	1.435

(b) Single volute

	$S_{pro\text{-}D}$		$S_{pro\text{-}T}$	
	impeller	volute	impeller	volute
water	0.001	0.003	0.566	4.456
573 K molten salt	0.003	0.005	0.663	4.660
723 K molten salt	0.001	0.002	0.498	2.981
838 K molten salt	0.001	0.001	0.496	2.200

4.1 Distribution of Turbulent Kinetic Energy

The turbulent kinetic energy (TKE) distributions of the impeller for the two molten salt pump schemes are shown in Fig. 5. The TKE describes the degree of turbulence of the pump. The distribution of TKE in the impeller channel is inhomogeneous despite the fact that the impeller is symmetrical in the circumferential direction. A region of large TKE is distributed on the impeller's blade suction surface and outlet edge. The interference between the volute and impeller is enhanced due to the circumferential symmetry of the double-volute scheme with two tongues. Therefore, the TKE in the impeller of the double-volute design is symmetrically distributed and more prominent.

The TKE distributions in the volutes of the two schemes are visualized in Fig. 6. Obviously, the turbulent energy dissipation is concentrated at the volute tongue, resulting in an immense TKE in this region, which is attributed to the rotor-stator interaction. The TKE is substantially higher near the single volute tongue than it

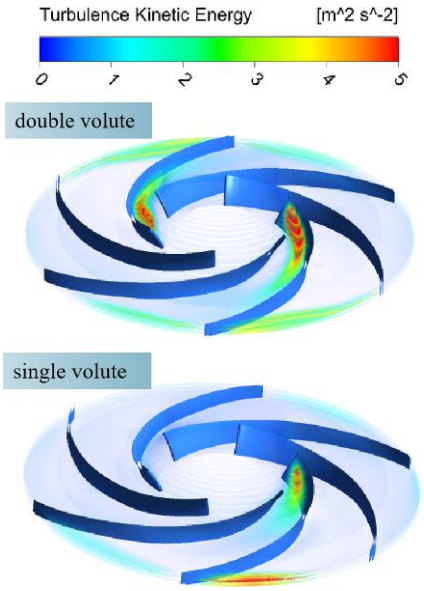

Fig. 5. TKE distribution in impeller (1.0q_v, 723 K molten salt).

is near the double volute tongue. This is owing to the double-volute scheme having two outlet pipes, and the flow rate of each outlet pipe is about half of that of the given flow rate. Thus, the double-volute design can reduce the turbulent dissipation in the volute, which verifies the entropy production in the double volute (see Table 3) is smaller than that in the single volute.

4.2 Distribution of Vortices with Q Criterion

Vortices are one of the primary reasons for enhanced turbulence intensity in the flow field. The higher turbulence intensity in the pump will result in more significant hydraulic loss. There are many methods for vortex identification, and the results obtained by these methods are not identical. Hitherto, no generalizable conclusions have been established for the universal applicability of any vortex identification method. The Q criterion is one of the methods for identifying vortices that have seen the most widespread use (Gao et al., 2020; Zhang et al., 2022). The Q criterion is expressed as

$$\nabla V = \begin{bmatrix} \frac{\partial u}{\partial x} & \frac{\partial u}{\partial y} & \frac{\partial u}{\partial z} \\ \frac{\partial v}{\partial x} & \frac{\partial v}{\partial y} & \frac{\partial v}{\partial z} \\ \frac{\partial w}{\partial x} & \frac{\partial w}{\partial y} & \frac{\partial w}{\partial z} \end{bmatrix} = A + B \tag{8}$$

$$A = \begin{bmatrix} \frac{\partial u}{\partial x} & \frac{1}{2}\left(\frac{\partial u}{\partial y} + \frac{\partial v}{\partial x}\right) & \frac{1}{2}\left(\frac{\partial u}{\partial z} + \frac{\partial w}{\partial x}\right) \\ \frac{1}{2}\left(\frac{\partial u}{\partial y} + \frac{\partial v}{\partial x}\right) & \frac{\partial v}{\partial y} & \frac{1}{2}\left(\frac{\partial v}{\partial z} + \frac{\partial w}{\partial y}\right) \\ \frac{1}{2}\left(\frac{\partial w}{\partial x} + \frac{\partial u}{\partial z}\right) & \frac{1}{2}\left(\frac{\partial w}{\partial y} + \frac{\partial v}{\partial z}\right) & \frac{\partial w}{\partial z} \end{bmatrix} \tag{9}$$

$$B = \begin{bmatrix} 0 & \frac{1}{2}\left(\frac{\partial u}{\partial y} - \frac{\partial v}{\partial x}\right) & \frac{1}{2}\left(\frac{\partial u}{\partial z} - \frac{\partial w}{\partial x}\right) \\ \frac{1}{2}\left(\frac{\partial v}{\partial x} - \frac{\partial u}{\partial y}\right) & 0 & \frac{1}{2}\left(\frac{\partial v}{\partial z} - \frac{\partial w}{\partial y}\right) \\ \frac{1}{2}\left(\frac{\partial w}{\partial x} - \frac{\partial u}{\partial z}\right) & \frac{1}{2}\left(\frac{\partial w}{\partial y} - \frac{\partial v}{\partial z}\right) & 0 \end{bmatrix} \tag{10}$$

$$Q = \frac{1}{2}\left(\|B\|_F^2 - \|A\|_F^2\right) \tag{11}$$

The area in which Q>0 indicates the vortex structure. In the above equations, $\| \ \|$ represents the Frobenius norm.

The vortex iso-surfaces in the impeller were obtained using the Q criterion (Q=30,000 s^{-2}; Gao et al., 2020). The results are shown in Fig. 7. Vortices can be found in the impeller flow channel of both schemes. The vortex iso-surfaces cover a larger area in the impeller of the double-volute scheme than in the single-volute scheme. Recall that vortex structures lead to more significant energy loss due to pressure fluctuations, and because the vortex structure occupies the channel space, the section area of the channel may be reduced. Therefore, the non-uniformity flow is enhanced in the impeller of the double-volute design. Further, the intense non-uniformity flow will affect the performance of the pump.

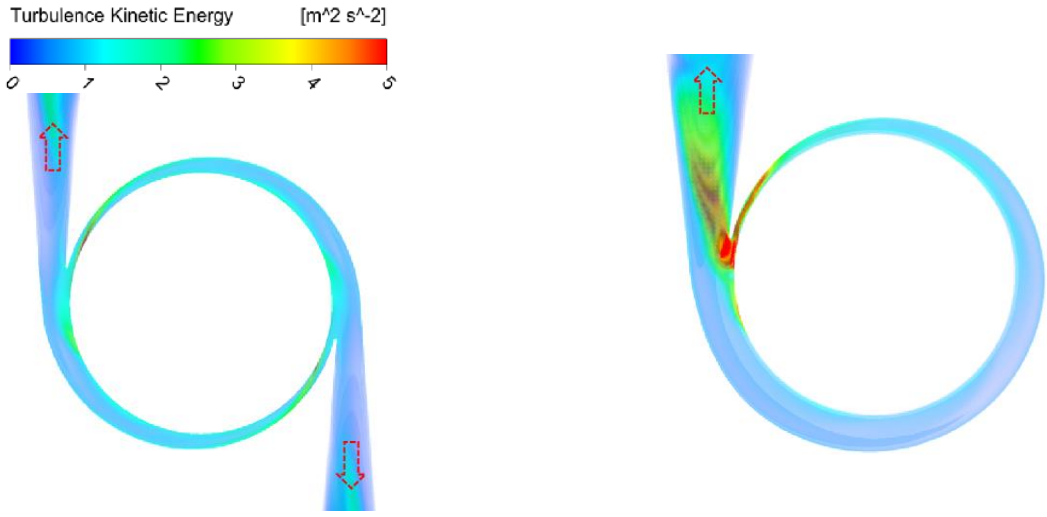

(a) Double volute (b) Single volute

Fig. 6. TKE distribution in volute (1.0q_v, 723 K molten salt).

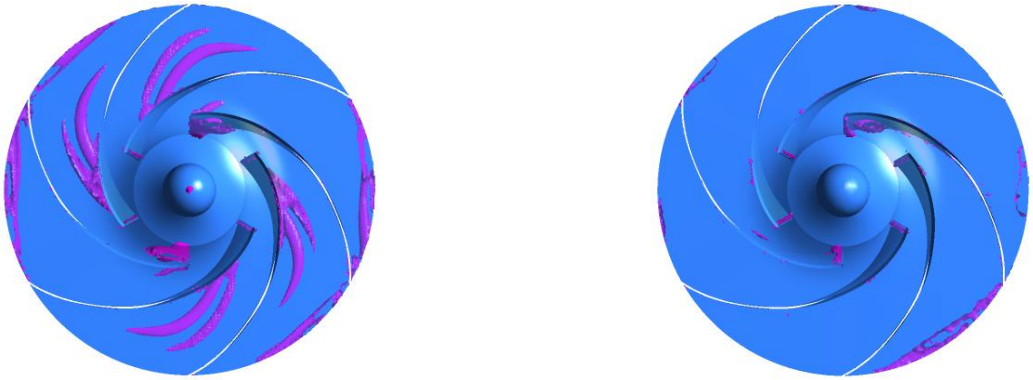

(a) Double volute (b) Single volute

Fig. 7. Three-dimensional vortex iso-surfaces in the impeller (Q=30,000 s^{-2}).

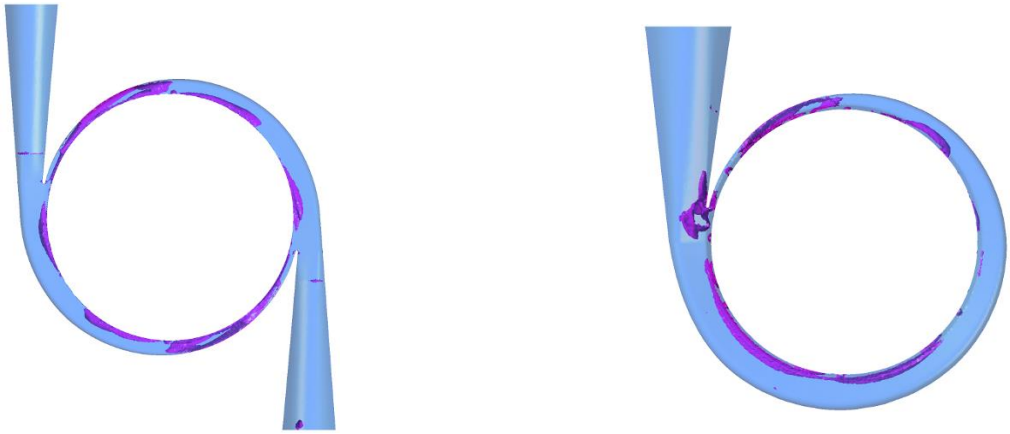

(a) Double volute (b) Single volute

Fig. 8. Three-dimensional vortex iso-surfaces in the volute (Q=30,000 s^{-2}).

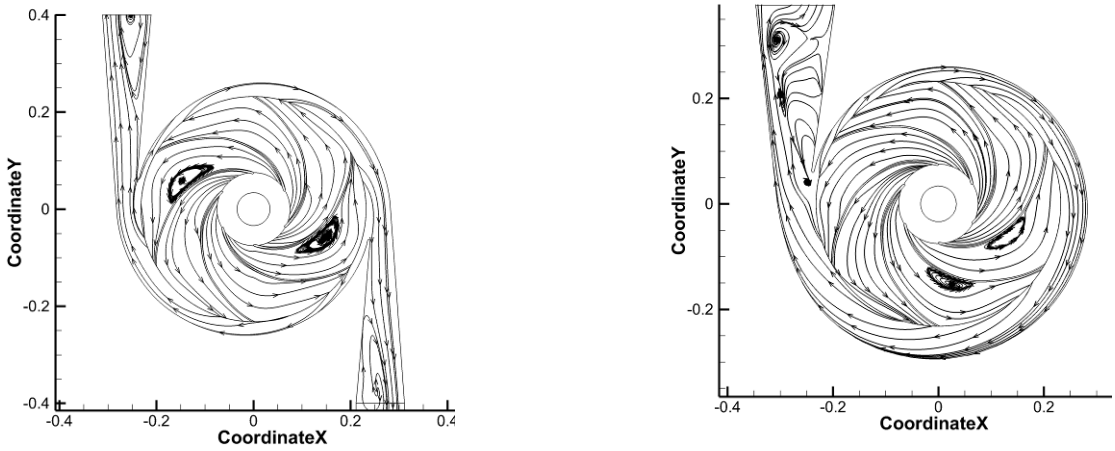

(a) Double volute (b) Single volute

Fig. 9. Streamline distribution in the molten salt pumps (1.0q_v, 723 K molten salt).

The vortex iso-surfaces in the volute were obtained using the Q criterion (Q=30,000 s^{-2}; Gao et al., 2020). The results are shown in Fig. 8. Like ordinary centrifugal pumps, the volute of the molten salt pump also has obvious vortexes. However, comparing the single-volute design with the double-volute design, it can be seen that the vortex iso-surfaces distribution in the volute is significantly different. There is an apparent vortex structure at the single volute tongue. The non-uniform flow in the volute is the crucial cause of energy loss. The vortex iso-surface is symmetrically distributed around the circumference in the double volute, and the vortex at the volute tongue is restrained by the double-volute structure, thus reducing the energy loss in the volute.

4.3 Distribution of Streamlines

The distributions of the streamlines in the two molten salt pumps are given in Fig. 9. There is an evident swirling flow in both the volute and impeller of the two pumps. The flow mode in the double-volute pump is circumferential symmetry because the double volute has a circumferential symmetry structure. The interesting

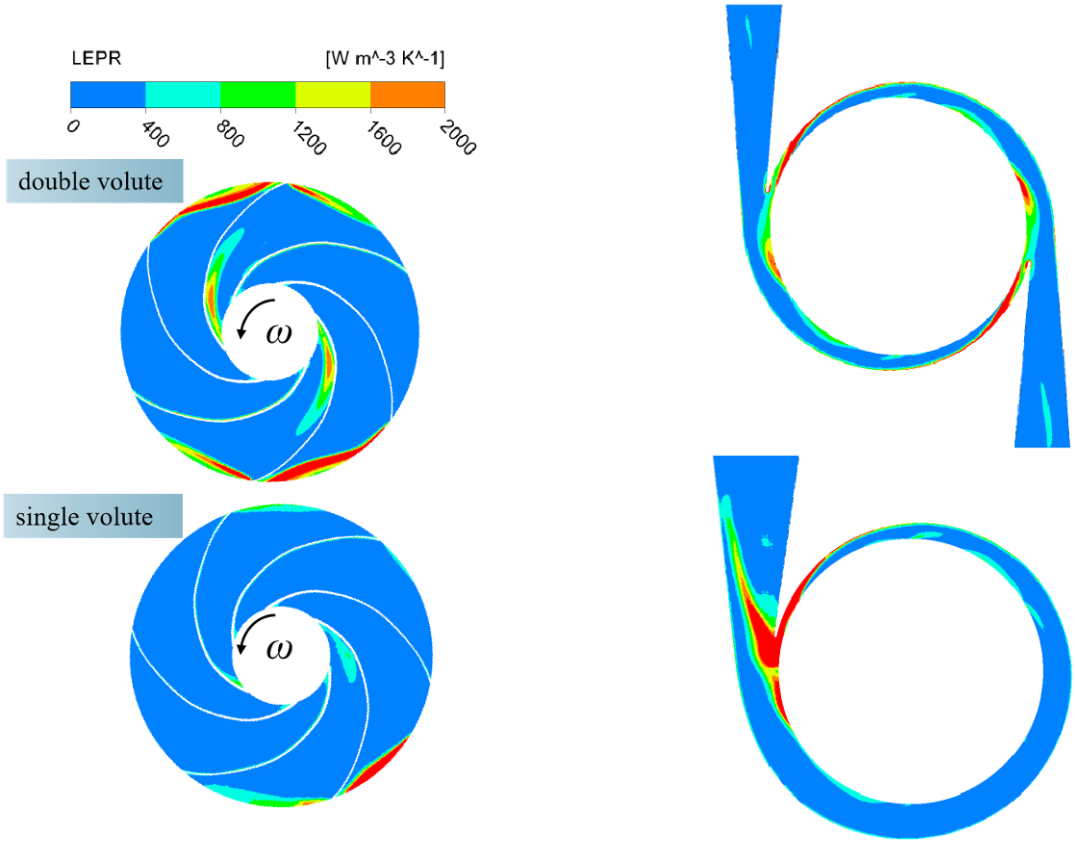

(a) Impeller (b) Volute

Fig. 10. LEPR distributions in impeller and volute (1.0q_v, 723 K molten salt).

phenomenon is that the swirling flow formed in the two pumps varies in scale and position. The swirling flow in the impeller is far away from the single-volute tongue, while the opposite is true in the impeller of the double-volute pump. As is evident, the distribution of streamlines in the double volute outlet is more regular than in the single volute outlet. Moreover, a swirling flow forms at the tongue of the single-volute pump.

4.4 Distribution of LEPR

The LEPR distribution in the impeller and volute serves as a pertinent indicator of the energy loss in molten salt pumps. To illustrate the correlation between the flow field and LEPR, the cross-sectional LEPRs in the two volute schemes at 1.0q_v and 723 K are displayed in Fig. 10.

The LEPR in the impeller is distributed at the outer edge and blade suction surface, as shown in Fig. 10(a). The distribution of LEPR in the impeller of the double-volute scheme is more significant than that of the single-volute scheme. The entropy production in the two volutes is principally generated at the volute tongues, as shown in Fig. 10(b). Although the double volute has two tongues, the LEPR at the single volute tongue is larger. The LEPR distributions in the volute and impeller of the double-volute scheme are symmetric in the circumferential direction. Figures. 4 and 10 indicate that the LEPR distributions in the impeller and volute channel of the two schemes are highly consistent with the TKE distribution. Therefore, it can be concluded that turbulent flow assumes a dominant role in entropy production.

5. FLUID–THERMAL–STRUCTURE COUPLING ANALYSIS

The stability of molten salt pumps is significantly impacted by the complicated unsteady flow and high temperature, which may also lead to rotor structural deformation. (Kumar et al., 2022). Therefore, coupling analysis of the multiple physical fields is necessary. Regarding the difficulty of establishing a high-temperature molten salt circulation system in the laboratory, fluid–structure coupling was used in this research (Liu et al., 2021).

5.1 Structural Simulation Scheme

(1) Thermal Analysis

For thermal analysis, it was assumed that the heat flowing into and out of the pump was equal and the pump system was in a thermally steady state. The following governing equation was used in the performance of the steady thermal analysis:

$$[K(T)]\{T\}=\{Q(T)\} \tag{12}$$

where $\{Q(T)\}$ represents the heat flow rate vector of the node; $\{T\}$ represents the temperature vector of the node; and $[K(T)]$ represents the heat transfer matrix.

(2) Stress Analysis

The Von Mises yield principle states that the dilatational strain energy density significantly impacts a material's yield failure. The following definition of the

Table 4 Physical properties of ZG1Cr13.

Physical property	Value
Density /kg/m^3	7 720
Poisson's ratio	0.281
Elastic modulus /GPa	219
Yield strength/ MPa	685
Coefficient of thermal expansion /K^{-1}	1.02×10^{-5}

Von Mises stress conforms to the fourth strength theorem:

$$\sigma_e = \sqrt{\frac{(\sigma_1-\sigma_2)^2+(\sigma_2-\sigma_3)^2+(\sigma_3-\sigma_1)^2}{2}} \tag{13}$$

where σ_i (i=1, 2, 3) represents the normal stress in the three directions of the structural element.

5.2 Computational Model, Loads, and Constraints

The nut, the shaft, and the impeller are the three components that make up the rotor. We consider an impeller outlet width of 16 mm, impeller diameter of 464.0 mm, and shaft length of 2,100 mm. The rotor components are fabricated from ZG1Cr13 martensitic stainless steel, and the properties are presented in Table 4.

As the pump operates, the rotor is subject to hydraulic loads, gravitational force, centrifugal force, and thermal stress. The simulations of heat transfer and flow were used to obtain the hydraulic load and thermal stress, which were then transmitted to the rotor via the interface between fluid and structure by utilizing the ANSYS Workbench software. After establishing the rotation angle speed of the impeller, an automated calculation of the centrifugal force load was carried out. The rotor component was constrained by the bearing. A cylindrical constraint was imposed on the surfaces of two segments of the shaft in contact with the bearing, as shown in Fig. 11. The grid scheme for the pump rotor is displayed in Fig. 12.

5.3 Radial Force Exerted on the Pump

The resultant radial force exerted on the volute and impeller under the two schemes as the pump operates over one period is displayed in Fig. 13. The position of impeller rotation is sketched in Fig. 13, where θ+X is the angle swept by the blade rotation. The rotor will bend under the action of the radial force. Although the bending degree is sometimes slight, there may be potential safety hazards as a result of the long-time operation. The rotation angle influences the radial force, which is attributed to the different hydraulic loads in the pump caused by the different positions of the impeller. The double-volute design is more symmetrical than the single-volute pump, which reduces the radial force by a large margin. Even the resultant radial force can almost be neglected, which is the original intention of the pump design.

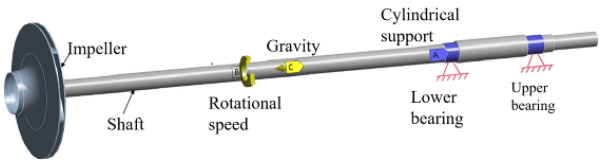

Fig. 11. Constraints and loads.

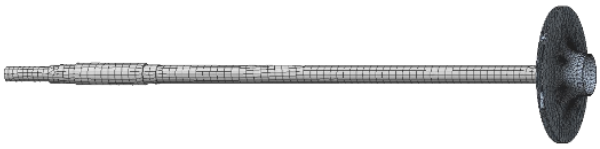

Fig. 12. Grid for the molten salt pump rotor.

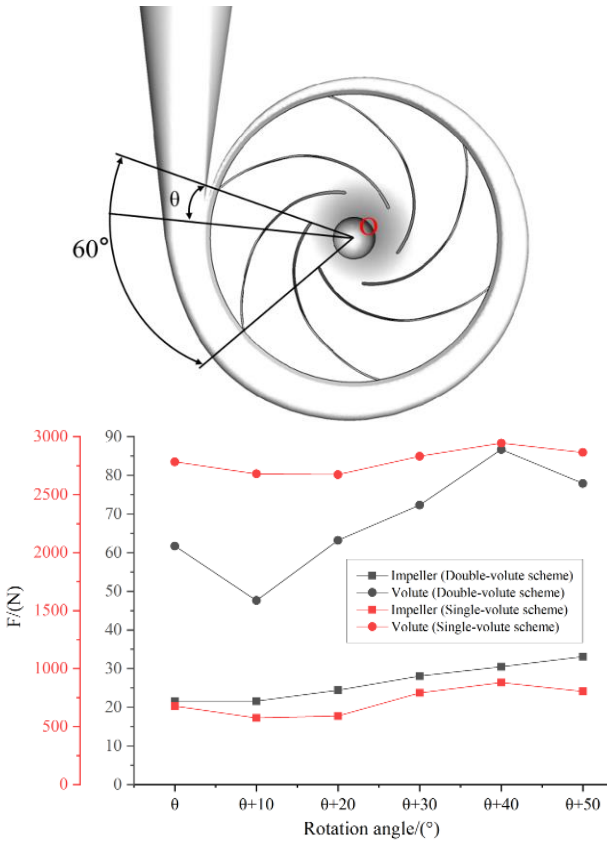

Fig. 13. Resultant radial force exerted on the volute and impeller (1.0q_v, 723 K molten salt).

5.4 Distributions of Stress and Deformation

The equivalent stress distributions in the rotor with the two molten salt pump schemes as the impeller rotates to θ+20°, as shown in Fig. 14. The similarities between the two schemes are evident. The equivalent stress of the impeller varies periodically along the circumferential direction, especially for the double-volute design. The equivalent stress for each blade channel gradually rises from the inlet to the outlet edge. Because of the action of torque converted through the shaft and the radial hydraulic force, the rotor experiences the maximum equivalent stress at the interface between the shaft and lower bearing in both schemes. The maximum equivalent stress on the impeller and shaft of the single-volute design is 213 MPa and 302 MPa, respectively, while the corresponding values for the double-volute pump are 224 MPa and 275 MPa. The maximum equivalent stress on

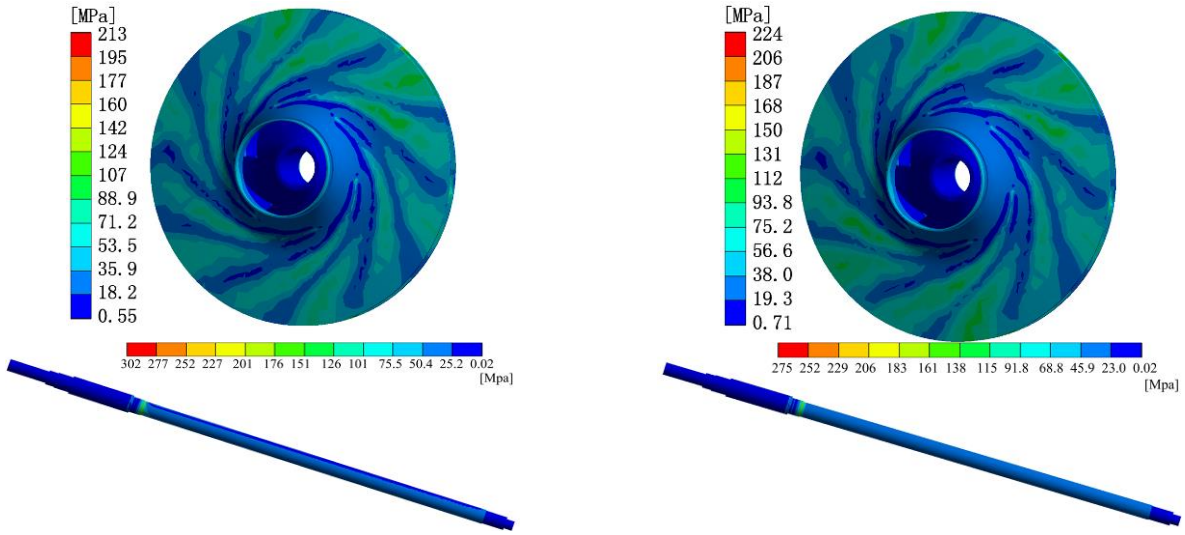

(a) Single volute (b) Double volute

Fig. 14. Equivalent stress of the impeller and shaft (1.0q_v, 723 K molten salt)

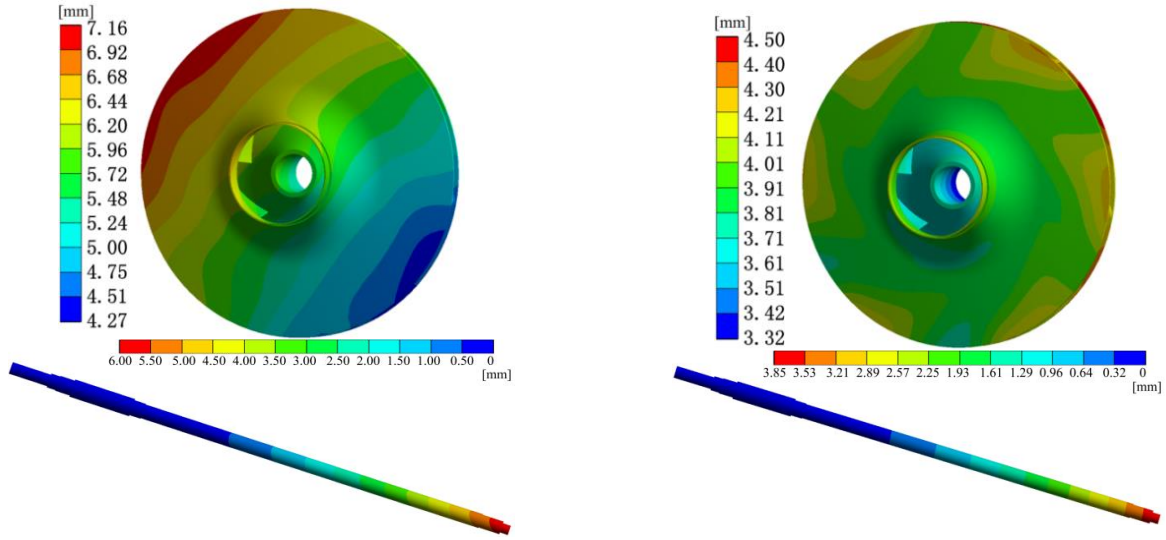

(a) Single volute (b) Double volute

Fig. 15. Deformation of the the impeller and shaft (1.0q_v, 723 K molten salt).

the shaft is significantly reduced using a double-volute design instead of a single-volute design. According to the relationship between material yield stress [σ_s], allowable stress [σ], and the safety factor n_s (n_s=[σ_s]/[σ]), the impeller and shaft of the single-volute pump have safety factors of 3.20 and 2.27, respectively, compared with 3.06 and 2.50 for the double-volute scheme. The rotors of both molten salt pump structures satisfy the structural strength requirements during operation.

The deformation distributions in the rotor are displayed in Fig. 15. It can be seen that the impeller is displaced along the radial direction, and the shaft exhibits bending and torsion. The impeller deformation magnitude of the single-volute scheme increases continuously along a single direction. In comparison, the impeller deformation of the double-volute scheme is symmetrically distributed around the circumference. The impeller's outer edge experiences the maximum deformation magnitude (7.16 mm for the single-volute pump and 4.50 mm for the double-volute pump). The shaft undergoes considerable bending and torsion, which can be ascribed to the centrifugal force load, resultant radial force load, and cylindrical constraint. The most significant amount of the shaft's deformation of two schemes takes place at the connection with the nut. The deformation then attenuates away from the impeller. In terms of the maximum deformation magnitude, the double-volute design improves the operational reliability of the molten salt pump.

6. CONCLUSIONS

(1) The double-volute pump satisfies the head and efficiency requirements for transporting molten salt. The local pulsating entropy production ($S_{pro\text{-}T}$) is a molten salt pump's primary source of local entropy production. While operating at 1.0q_v with 723 K molten salt, the double-volute design reduces the total local entropy production by roughly 19% compared to the single-volute design.

(2) The LEPR and flow field distributions of the two schemes show that the LEPR positively correlates with the complex flow, and the TKE and LEPR are formed in the same region of the pumps. The double-volute scheme reduces the complexity of the flow in the volute and increases the non-uniformity flow in the impeller, which makes the LEPR in the pump modified with the same tendency.

(3) The symmetrical double volute can reduce the resultant radial force exerted on the pump. In both structures considered in this paper, the maximum equivalent stress of the shaft and impeller satisfies the structural strength requirements during operation. The double-volute scheme diminishes the potential for rotor failure compared to the single-volute pump.

ACKNOWLEDGEMENTS

This study was supported by the Natural Science Foundation of Jiangsu Province (Grant No. BK20201315).

CONFLICT OF INTEREST

The authors declare there is no conflict.

AUTHORS CONTRIBUTION

Q. Li: Conceptualization, Methodology, Software, Validation, Formal analysis, Writing –original draft.

R. Zhang: Methodology, Data curation, Funding acquisition, Writing – review & editing.

H. Xu: Methodology, Resources, Supervision.

REFERENCES

Barth, D. L., Pacheco, J. E., Kolb, W. J., & Rush, E. E. (2002). Development of a high-temperature, long-shafted, molten-salt pump for power tower applications. *Journal of Solar Energy Engineering*, 124(2), 170–175. https://doi.org/10.1115/1.1464126

Cheng, W. J., Gu, B. Q., & Shao, C. L. (2017a). A numerical study on the steady flow in molten salt pump under various conditions for improved hydraulic performance. *International Journal of Numerical Methods for Heat and Fluid Flow*, 27(8), 1870–1886. https://doi.org/10.1108/HFF-06-2016-0238

Cheng, W. J., Gu, B. Q., Shao, C. L., & Wang, Y. (2017b). Hydraulic characteristics of molten salt pump transporting solid-liquid two-phase medium. *Nuclear Engineering and Design*, 324, 220–230. https://doi.org/10.1016/j.nucengdes.2017.08.036

Cheng, W. J., Shao, C. L., & Zhou, J. F. (2019). Unsteady study of molten salt pump conveying mediums with different viscosities. *International Journal of Heat and Mass Transfer*, 137, 174–183. https://doi.org/10.1016/j.ijheatmasstransfer.2019.03.095

Duan, L., Wu, X. L., Ji, Z. L. & Fang, Q. X. (2015). Entropy generation analysis on cyclone separators with different exit pipe diameters and inlet dimensions. *Chemical Engineering Science*, 138, 622–633. https://doi.org/10.1016/j.ces.2015.09.003

Egusquiza, E., Valero, C., Huang, X. X., Jou, E., Guardo, A., & Rodriguez, C. (2012). Failure investigation of a large pump-turbine runner. *Engineering Failure Analysis*, 23, 27–34. https://doi.org/10.1016/j.engfailanal.2012.01.012

Fei, Z. D., Zhang, R., Xu, H., Feng, J. G., Mu, T. & Chen, Y. H. (2022). Energy performance and flow characteristics of a slanted axial-flow pump under cavitation conditions. *Physics of Fluids*, 34(3), 035121. https://doi.org/10.1063/5.0085388

Gao, Z. W., Wang, J., Liu, Z. X., Wei, Y. D., Wang, J. Y., & Mao, Y. (2020). Effects of different inlet structures on the flow field of cyclone separators. *Powder Technology*, 372, 519–531. https://doi.org/10.1016/j.powtec.2020.06.014

Gu, J. R., Gao, B., Ni, D., Li, C., & Zhong, Y. M. (2022). Investigation on the unsteady pressure pulsations and related vortical structures in a molten salt pump. *Energy Science and Engineering*, 10(8), 2858–2876. https://doi.org/10.1002/ese3.1175

Gu, Y. D., Pei, J., Yuan, S. Q., Wang, W. J., Zhang, F., Wang, P., Appiah, D., & Liu, Y. (2019). Clocking effect of vaned diffuser on hydraulic performance of high-power pump by using the numerical flow loss visualization method. *Energy*, 170, 986–997. https://doi.org/10.1016/j.energy.2018.12.204

Huan, Y. Y., Liu, Y. Y., Li, X. J., Zhu, Z. C., Qu, J. T., Zhe, L., & Han, A. D. (2021). Experimental and numerical investigations of cavitation evolution in a high-speed centrifugal pump with inducer. *Journal of Hydrodynamics*, 33(1), 140-149. https://doi.org/10.1007/s42241-021-0006-z

Jin, Y. X., Zhang, D. S., Song, W. W., Shen, X., Shi, L., & Lu, J. X. (2022). Numerical study on energy conversion characteristics of molten salt pump based on energy transport theory. *Energy*, 244, 122674. https://doi.org/10.1016/j.energy.2021.122674

Kang, C., Li, Q., Li, M. Y., & Teng, S. (2020). Deposition of solid particles exposed to the suction of dual pumps in the tank of a pumping station. *Powder Technology*, 361, 727–738. https://doi.org/10.1016/j.powtec.2019.11.049

Kang, C., Lu, C., Seah, K. G. & Zhang, W. (2022). Cavitation characteristics during startup process of a condensate pump with splitter blades. *Journal of Applied Fluid Mechanics*, 15(4),1099-1109. https://doi.org/10.47176/jafm.15.04.1082

Kang, C., Mao, N., Pan, C., Zhu, Y., & Li, B. (2017). Effects of short blades on performance and inner flow characteristics of a low-specific-speed

centrifugal pump. *Proceedings of the Institution of Mechanical Engineers, Part A: Journal of Power and Energy*, 231(A4), 290–302. https://doi.org/10.1177/0957650917695672

Kang, C., Zhu, Y., & Li, Q. (2020). Effects of hydraulic loads and structure on operational stability of the rotor of a molten-salt pump. *Engineering Failure Analysis*, 117, 104821. https://doi.org/10.1016/j.engfailanal.2020.104821

Kock, F., & Herwig, H. (2004). Local entropy production in turbulent shear flows: A high-Reynolds number model with wall functions. *International Journal of Heat and Mass Transfer*, 47(10), 2205–2215. https://doi.org/10.1016/j.ijheatmasstransfer.2003.11.025

Kock, F., & Herwig, H. (2005). Entropy production calculation for turbulent shear flows and their implementation in CFD codes. *International Journal of Heat and Fluid Flow*, 26(4), 672–680. https://doi.org/10.1016/j.ijheatfluidflow.2005.03.005

Kumar, M., Venkateshwaran, A., Kumar, M. S. S. P., Sreekanth, M., Jebaseelan, D., & Sivakumar, R. (2022). Strength analysis of a regenerative flow compressor and a pump based on fluid-structure coupling. *Materials Today: Proceedings*, 51, 1619–1624. https://doi.org/10.1016/j.matpr.2021.10.477

Li, Q., Kang, C., Teng, S., & Li, M. Y. (2019). Optimization of tank bottom shape for improving the anti-deposition performance of a prefabricated pumping station. *Water*, 11(3), 602. https://doi.org/10.3390/w11030602

Lin, T., Zhu, Z. C., Li, X. J., Li, J., & Lin, Y. P. (2021). Theoretical, experimental, and numerical methods to predict the best efficiency point of centrifugal pump as turbine. *Renewable Energy*, 168(5), 31-44. https://doi.org/10.1016/j.renene.2020.12.040

Liu, C., Zhou, J. Z., Duan, R., Liu, Y., & He, Y. X. (2021). Fluid-structure coupling analysis of inlet ball valve on pumped-storage power station under extreme conditions. *Journal of Physics: Conference Series*, 1983(1), 012012. https://doi.org/10.1088/1742-6596/1983/1/012012

Moshfeghi, M., Song, Y. J., & Yong, H. X. (2012). Effects of near-wall grid spacing on SST-K-ω model using NREL Phase VI horizontal axis wind turbine. *Journal of Wind Engineering and Industrial Aerodynamics*, 107–108, 94–105. https://doi.org/10.1016/j.jweia.2012.03.032

Pei, J., Yuan, S. Q., & Yuan, J. P. (2014). Dynamic stress analysis of sewage centrifugal pump impeller based on two-way coupling method. *Chinese Journal of Mechanical Engineering*, 27(2), 369–375. https://doi.org/10.3901/CJME.2014.02.369

Peiró, G., Gasia, J., Miró, L., Prieto, C. & Cabeza, L. F. (2017). Influence of the heat transfer fluid in a CSP plant molten salts charging process. *Renewable Energy*, 113, 148–158. https://doi.org/10.1016/j.renene.2017.05.083

Shao, C. L. & Zhao, Y. (2017). Numerical study of the dimensionless characteristics and modeling experiment of a molten salt pump that transports viscous fluids. *International Journal of Numerical Methods for Heat and Fluid Flow*, 27(9), 2131–2153. https://doi.org/10.1108/HFF-07-2016-0267

Shao, C. L., He, A. X., Zhang, Z. Y. & Zhou, J. F. (2019). Study on the transition process of a molten salt pump transporting media with crystalline particles by modeling test and numerical simulation. *International Journal of Numerical Methods for Heat and Fluid Flow*, 29(9), 3263–3289. https://doi.org/10.1108/HFF-12-2018-0807

Shao, C. L., Zhou, J. F. & Cheng, W. J. (2015). Experimental and numerical study of external performance and internal flow of a molten salt pump that transports fluids with different viscosities. *International Journal of Heat and Mass Transfer*, 89, 627–640. https://doi.org/10.1016/j.ijheatmasstransfer.2015.05.087

Smith, D. C., Rush, E. E., Matthews, C. W., Chavez, J. M., & Bator, P. A. (1994). Operation of Large-Scale Pumps and Valves in Molten Salt. *Journal of Solar Energy Engineering*, 116(3), 137–141. https://doi.org/10.1115/1.2930072

Teng, S., Kang, C. & Zhou, M. (2020). Hydraulic characteristics and structural stability of the rotor of a molten-salt pump. *Journal of Applied Science and Engineering*, 23(1), 117–128. https://doi.org/10.6180/JASE.202003_23(1).0013

Yu, A., Tang,Y. B., Tang, Q. H., Cai, J. G., Zhao, L. & Ge, X. F. (2022). Energy analysis of Francis turbine for various mass flow rate conditions based on entropy production theory. *Renewable Energy*, 183, 447–458. https://doi.org/10.1016/j.renene.2021.10.094

Zhang, H. H., You, H. L., Lu, H. S., Li, K., Zhang, Z. Y. & Jiang, L. X. (2020). CFD-rotordynamics sequential coupling simulation approach for the flow-induced vibration of rotor system in centrifugal pump. *Applied Sciences*, 10(3), 1186. https://doi.org/10.3390/app10031186

Zhang, Z. H., Dong, S. J., Jin, R. Z., Dong, K. J., Hou, L. A. & Wang, B. (2022). Vortex characteristics of a gas cyclone determined with different vortex identification methods. *Powder Technology*, 404, 117370. https://doi.org/10.1016/j.powtec.2022.117370

Zhou, H., Shi, H., Lai, Z. Y., Zuo, Y. H., Hu, S. H. & Zhou, M. X. (2020). Migration and phase change study of leaking molten salt in tank foundation material. *Applied Thermal Engineering*, 170, 114968. https://doi.org/10.1016/j.applthermaleng.2020.114968